Acta Geotechnica
https://doi.org/10.1007/s11440-018-0676-z

RESEARCH PAPER

Measurement of the deformation of sand in a plane strain compression experiment using incremental digital image correlation

Pengpeng Wang[1,2] · Yong Sang[3,4] · Longtan Shao[1,2] · Xiaoxia Guo[1,2]

Received: 13 November 2017 / Accepted: 2 May 2018

Abstract
This work presents the results from a series of plane strain compression experiments on medium-density sands. In these experiments, a new type of plane strain experimental apparatus and the incremental reliability-guided digital image correlation (RG-DIC) technique are used to research the localized deformation of sand specimens. The new apparatus can reduce the influence of boundary constraints in the experiments. The RG-DIC technique can not only obtain the full-field deformation distribution on the surface of sand specimens to analyse the evolution of the shear band in sand but can also determine the characteristics of the shear band, such as its inclination and thickness. Additionally, a methodology applying bifurcation and statistics has been devised to estimate the moments when the shear band begins and penetrates. These two moments can divide the compression process into three parts: pre-failure, in-failure and post-failure. According to an analysis of the deformation and assumptions regarding the plane strain model, the localized volume can also be estimated. The experimental results indicate that the RG-DIC technique performs well in geotechnical tests of large-scale deformation.

Keywords Bifurcation · Digital image correlation · Localized deformation · Plane strain experimental apparatus

1 Introduction

Failure in soils is associated with the formation of shear bands. To properly interpret and quantify the basic responses of soils to shear bands, such as stress–strain and volumetric conditions at failure, shear band behaviour has long been an important issue and has been analysed by many scholars. Accurate experimental data and analytic results can provide the crucial information for extrapolating predictability to shear band behaviour and establishing accurate theories. Since the strain localization theory based on the results of an analysis of the evolution of the shear band was proposed by Thomas [23], a variety of measurement techniques and a lot of work have been exploited to quantify local strain behaviour and the physical characteristics of shear bands, such as thickness, inclination and shear band patterns. X-ray computed tomography (CT) was applied to research the strain localization and void ratio evolution in sand [3, 4], and more recently, high-resolution (micro-X-ray) computed tomography (μCT) and 3-D measurement techniques have been used to evaluate the complex localization patterns in specimens and their volumetric deformation [1, 8, 10]. Using an epoxy-hardened technique, Jang [9] studied the microstructure of failed sand specimens. The method using microscopic images of thin slices of soil material prepared from epoxy-hardened specimens can reveal quantitative changes in particle orientations within the samples and be used to analyse the local void

✉ Longtan Shao
shaolt@hotmail.com; shaolongtan@126.com

1 State Key Laboratory of Structural Analysis for Industrial Equipment, Dalian University of Technology, Dalian District, Dalian City 116024, Liaoning Province, China

2 Department of Engineering Mechanics, Dalian University of Technology, Room 308, NO. 2, Ling Gong Road, Dalian City 116024, Liaoning Province, China

3 Key Laboratory for Precision and Non-Traditional Machining Technology, Ministry of Education, Dalian University of Technology, Dalian District, Dalian City 116024, Liaoning Province, China

4 School of Mechanical Engineering, Dalian University of Technology, Dalian 116024, Liaoning, China

Published online: 11 May 2018

ratio distribution. In recent years, several scholars have evaluated shear bands and their physical characteristics with a focus on the measurement of physical displacements using digital image measuring (DIM) techniques. Typically, in these methods, spaced markers, grid points or random speckles are painted on the specimen membrane, which can be caught by a digital camera. Although these methods only capture the surface deformation of specimens, they can be used to measure the deformation on the surface of specimens throughout testing. They are also useful for quantifying stress–strain behaviour, local deformation and shear band evolution [5, 16–19, 27, 28]. Feature matching in DIM involves extracting distinctive invariant features from images, which can be utilized to realize reliable matching between different views of a scene or object [12]. More discrete sampling points can provide more accurate modelling. However, thus far, feature matching has not been able to overcome the limitations that arise from using relatively few feature points. Digital image correlation (DIC) measurement technology is one of the methodologies in DIM that was proposed and applied by Sutton in the early 1980s [15]. Since then, an enormous amount of experimental research utilizing this method has been performed worldwide [6, 18, 20]. DIC is a robust, non-contact and non-interferometric method for full-field shape, motion and deformation measurements [2, 21, 25]. One of the important advantages of DIC is that the grey value of every pixel in the region of interest (ROI) of the digital image is utilized. Therefore, this methodology can provide much closer spacing and more points that are more suitable for the measurements of full-field motion, shape and deformation than those provided with feature matching. Recently, large deformation measurement of DIC technique has been developed [6, 13], and the application of this technology has been further extended.

The present paper describes a plane strain compression experimental study of medium-density sand in a new type of plane strain testing apparatus. Combining the full-field measurement of DIC technology, this method provides a convenient means to quantitatively analyse the onset, development and failure state of the shear band in the plane strain compression experiment. The localized deformation obtained by DIC can be used to analyse soil behavioural characterization, such as localized volumetric evolutions and localized stress–strain behaviour, both inside and outside the shear band. Based on statistics and the bifurcation phenomenon, a methodology has been devised to estimate the moments when the shear band begins and penetrates. Additionally, the shear band inclination and thickness can be easily obtained from the deformation field. The results illustrate that DIC is a useful methodology not only in geotechnical testing but for guiding soil behavioural models and DIC use in soil testing.

2 Experimental apparatus

Experiments were conducted in a new type of plane strain testing apparatus designed by our laboratory, The State Key Laboratory of Structural Analysis for Industrial Equipment in Dalian University of Technology. The schematic diagram of specimen configuration is conceptually depicted in Fig. 1. The plane strain testing apparatus is depicted in Fig. 2. The dimensions of a cubic specimen (nominal dimensions) are $120 \times 60 \times 100$ mm ($H/W = 2$). The specimen is wrapped in a black latex membrane; the front and back of specimen are mounted between two panes of tempered glass that inhibit strain in the out-of-plane direction, ε_2; the pressure in the direction, σ_1, is provided by a servomotor and ball screw system. The improvement provided by the instrument is mainly reflected in the loading mode in the direction of σ_3, which adopts flexible loading method. The traditional plane strain testing apparatus primarily adopts rigid boundaries. In this instrument, the two sidewalls of the specimen are pressed between two flexible pressure vessels. The flexible pressure vessels are made of latex membrane and filled with air-free water (Figs. 1, 2). The pressure of the air-free water can precisely controlled by a hydraulic pressure control apparatus between 0 and 400 kPa in the direction of σ_3. Flexible pressure vessels reduce the sliding friction of the boundary because the soft latex membrane vessels do not undergo shear stress, providing a closer simulation of the real circumstances of the boundaries of the soil material. To demonstrate that the flexible pressure vessels can reduce the influence of the boundary constraint, the specimens were loaded under a confining pressure of 100 kPa and

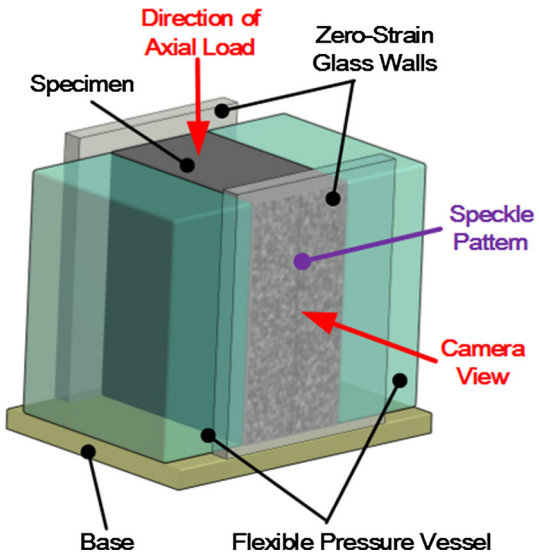

Fig. 1 Stress conditions of specimens and surrounding hardware in the new type of plane strain testing apparatus

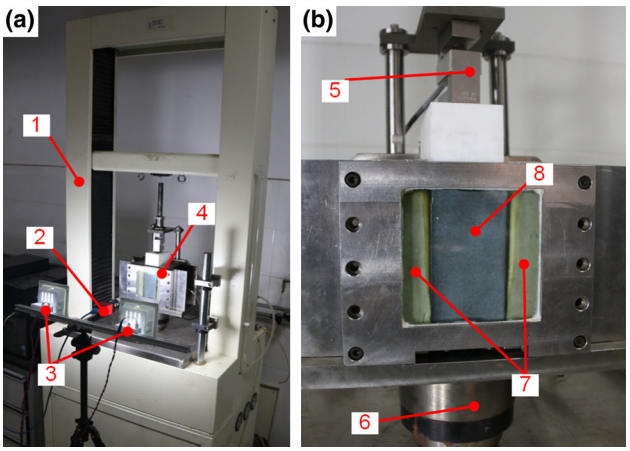

Fig. 2 Components of the measurement system. **a** The layout of the apparatus. **b** The photograph of the pressure cell 1—testing machine; 2—digital camera; 3—fluorescent lamps; 4—pressure cell; 5—the top load cell; 6—the bottom load cell; 7—flexible pressure vessels; 8—Specimen

vacuum confinement. Figure 3 presents the loading curves for these two conditions. Because of the limited constraints, the loading curve under the vacuum confinement is more smooth and stable; in particular, the loading force is almost invariable in the post-failure state. However, the two loading curves are very similar. The calibration experiments indicate the utility of flexible pressure vessels. In the experiments, the specimens' sidewall interfaces are also lubricated with silicon oil to minimize contact frictional force. Two load cells are mounted above and below the specimen. Two pressure sensors are arranged to measure the pressure of the flexible pressure vessels and the pore pressure. A Linear Variable Differential Transformer (LVDT) displacement transducer is arranged to measure axial deformation to assist the DIC measurement system.

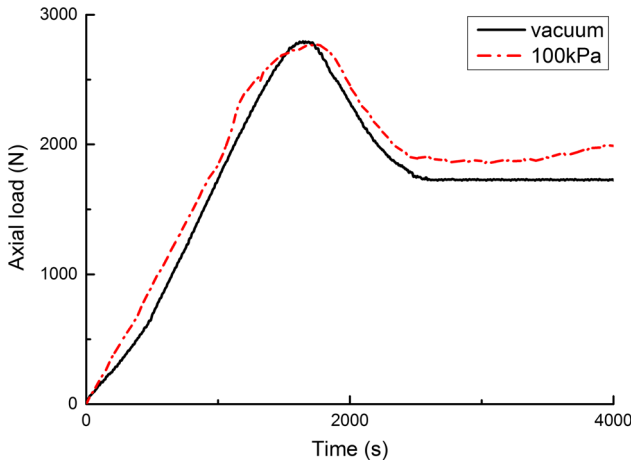

Fig. 3 Loading processes under confining pressure of 100 kPa and vacuum confinement

The sand used for the tests is Fujian (China) standard sand. The grain size distribution curve is shown in Fig. 4, and the properties of this sand are listed in Table 1. This medium-density sand specimen was prepared using a vibratory approach and was divided into four layers. Displacement control was applied for loading on the specimen at a vertical rate of 0.2 mm/min. These specimens were assigned numbers T-1–T-6 and tested under three different confining pressure conditions—50, 100 and 150 kPa—for the three specimens of each confining pressure. Specimens T1 to T3 were tested with an undrained test, in which they were permeated with carbon dioxide, back-pressure saturated, consolidated uniformly and sheared under undrained conditions. Specimens T4–T6 were tested under completely dry conditions (Table 2). Considered the loading vertical rate, images of the specimens were captured at time intervals of 5 s during the test.

3 The calibration of digital image correlation (DIC) and measurement of large deformation

With the development of DIC technology, the algorithm has been greatly improved by several researchers to provide increased calculation speed and achieve high precision. To date, DIC technology has been commonly used as a flexible tool for deformation measurement in the field of experimental solid mechanics. The fundamental principle has been described in several literatures [6, 11, 22].

An important step in DIC technology is to track the subset between the reference subset and current subset. This step is carried out by comparing greyscale values at the reference subset points with greyscale values at the current subset points. To estimate the degree of similarity between the two subsets, various correlation functions are

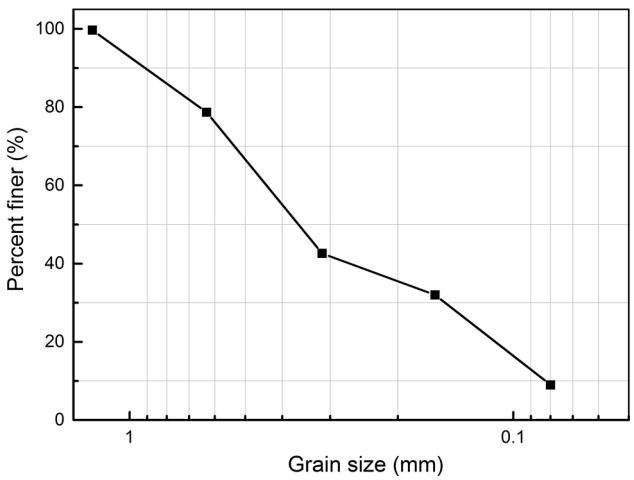

Fig. 4 Grain size distribution curve for Fujian (China) standard sand

Table 1 Properties of experimental sands

Sands	ρ_d	D_{50}	e_{max}	e_{min}	D_r (%)	G_s	C_u	C_c
Fujian standard sand	1.57 g/cm^3	0.37 mm	1.04	0.60	87	2.65	5.49	0.68

Table 2 Shear band inclinations and thickness of calculation and measurement

Test	Confining pressure (kPa)	Test conditions	ϕ' (°)	ψ (°)	β_C (°)	β_R (°)	β_A (°)	β (°)	T (D_{50})
T-1	50	CU	42.5	7	66.3	46	57.4	60	13
T-2	100	CU		6		45.5	57.1	61	12
T-3	150	CU		7		46	57.4	61	12
T-4	50	–	41	13	65.5	51.5	58.5	58	18
T-5	100	–		11		50.5	58	58	17
T-6	150	–		16		53	59.3	55	14

CU indicates that the specimen was tested under consolidated undrained conditions; – indicates that the specimen was tested under dry conditions

defined, such as Cross-Correlation (CC), Sum of Absolute Differences (SAD) algorithm [24], Sum of Squared Difference (SSD) and Zero-mean Normalized Sum of Squared Difference (ZNSSD) [14, 26]. Because the ZNSSD is insensitive to the scale and offset changes in illumination lighting fluctuations, the robust ZNSSD is commonly used as the error measure for subset matching. In this paper, the ZNSSD is selected as the correlation criterion. After subset matching is completed, cubic spline interpolation is generally used for subpixel intensity interpolation. According to the principle of the DIC algorithm, the DIC code was edited and compiled by our laboratory. It is necessary to confirm the algorithm precision. To avoid the image noise from the camera, a speckle pattern image (400 × 400 pixels) was drawn with MATLAB (Fig. 5a). The compression process of gradual change from the top to the bottom was simulated. In the deformed image, the bottom of the speckle pattern image had no displacement value and the top moved down two pixels. The displacement value increased uniformly from the bottom to the top. Figure 5b presents the displacement field in the ROI according to the DIC method (the lower left corner of ROI is the origin of the XY plane). The displacement value for each line in the deformed image is the same. Comparing the average values for each line and the ideal value, the absolute value of error is shown in Fig. 5c. The result indicates that the DIC method can provide subpixel resolution. The error is smaller than 0.01 pixel.

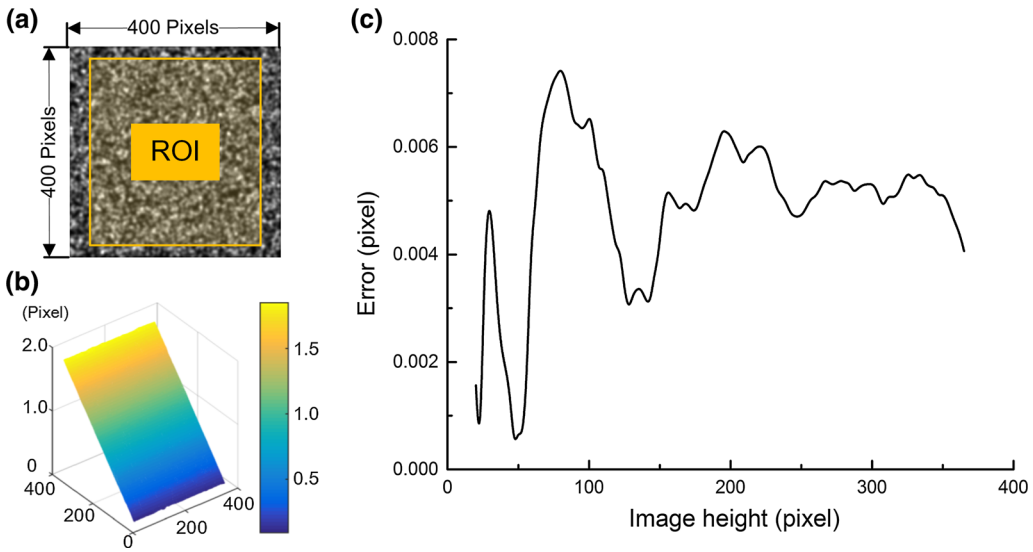

Fig. 5 **a**–**c** Calibration of DIC algorithm. **a** Simulated diagram. **b** The displacement distribution obtained by DIC. **c** The absolute error between the measured value and the true value

The evolution of the shear band was observed in a plane strain compression experiment. The axial strain exceeded 12% in the global measure, and the local deformation was more than 37%. The distribution of deformation is highly heterogeneous and complex, including the movement and rolling of sand. In the conventional DIC algorithm, the first image is considered as the reference image and all the deformed images are compared with the first image to extract the deformation information. The deformation cannot be revealed by the conventional DIC algorithm because of the large difference among images. This shortcoming is the so-called decorrelation effect. To resolve the "decorrelation effect", it is necessary to update the reference image at a given time with the increase of deformation. However, frequently updating the reference image would unavoidably accumulate large additional errors in the deformation measurement [7, 13]. Therefore, a key incremental reliability-guided digital image correlation (RG-DIC) technique has been used to maintain the measurement accuracy and reduce the updating of reference images to the minimum number required [13]. In the incremental RG-DIC technique, several seed points are defined in the original reference image. If all correlation coefficients of seed points are smaller than the preset threshold during matching in the deformed images (according to the ZNSSD criterion, a smaller correlation coefficient provides better matching), no decorrelation effect is present. Otherwise, the image preceding the current deformed image is selected as an updated reference image to continue correlation analysis.

In the direction of the camera view, the front of the specimen is sprayed with white paint. The white paint and black latex membrane constitute the artificial speckle pattern. The high-resolution speckle pattern digital images on the front of the specimen are captured using a Pike F-100B/C, which is a 1 megapixel camera for sophisticated applications and has a CCD sensor. The resolution of the camera is 1000×1000 pixels. In testing, one pixel equals approximately 0.11 mm (according to the field of camera in every test). Two 20-W fluorescent lamps provided continuous illumination of the specimen surface (Fig. 2). In every test, approximately 800 photographs were computed and matched. Because large deformations hinder matching, the algorithm cannot continue beyond the first one hundred photographs when using the conventional DIC algorithm. When using the RG-DIC, all photographs can be computed and only eight or nine reference images are updated automatically. Figure 6 presents the procedures for realizing the RG-DIC technique.

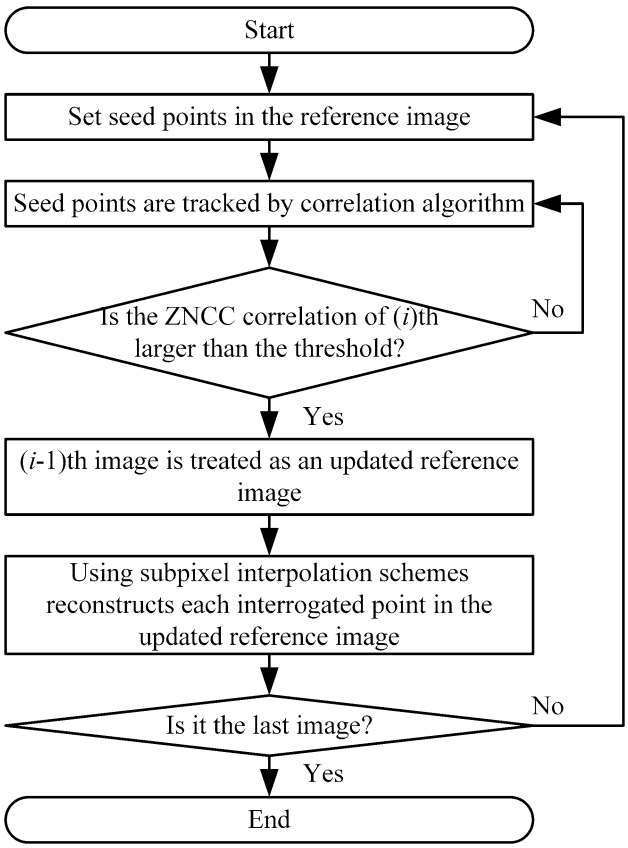

Fig. 6 Procedures for realizing the RG-DIC technique

4 Experimental results

4.1 Incremental specimen deformation

The DIC measurement technique can be used to directly obtain the vertical strain and the horizontal strain in plane strain compression experiment. Additionally, the shear strain also can be calculated from those two strains. The three types of strain can be utilized to qualitatively evaluate the deformation of a specimen and the evolution of shear bands. Here, the vertical deformation of sand specimens at several typical moments was taken as an example to analyse the evolution of shear bands. Figure 7a–f presents the incremental subset displacement (unit: mm) contours and strain (unit: ε) distribution diagrams of the measured DIC algorithm through the course of test T2, which are calculated and viewed from Lagrangian perspective. Figure 7a–e corresponds to five moments (five red points) shown in Fig. 7f. In each figure, the left figure indicates the vertical displacement contours (V) and the right indicates its vertical strain distribution (ε), respectively. The direction of compression is positive. For this test analysis, subset sizes are 21×21 pixels and subset points space two pixels. Approximately 42,000 points are used for the

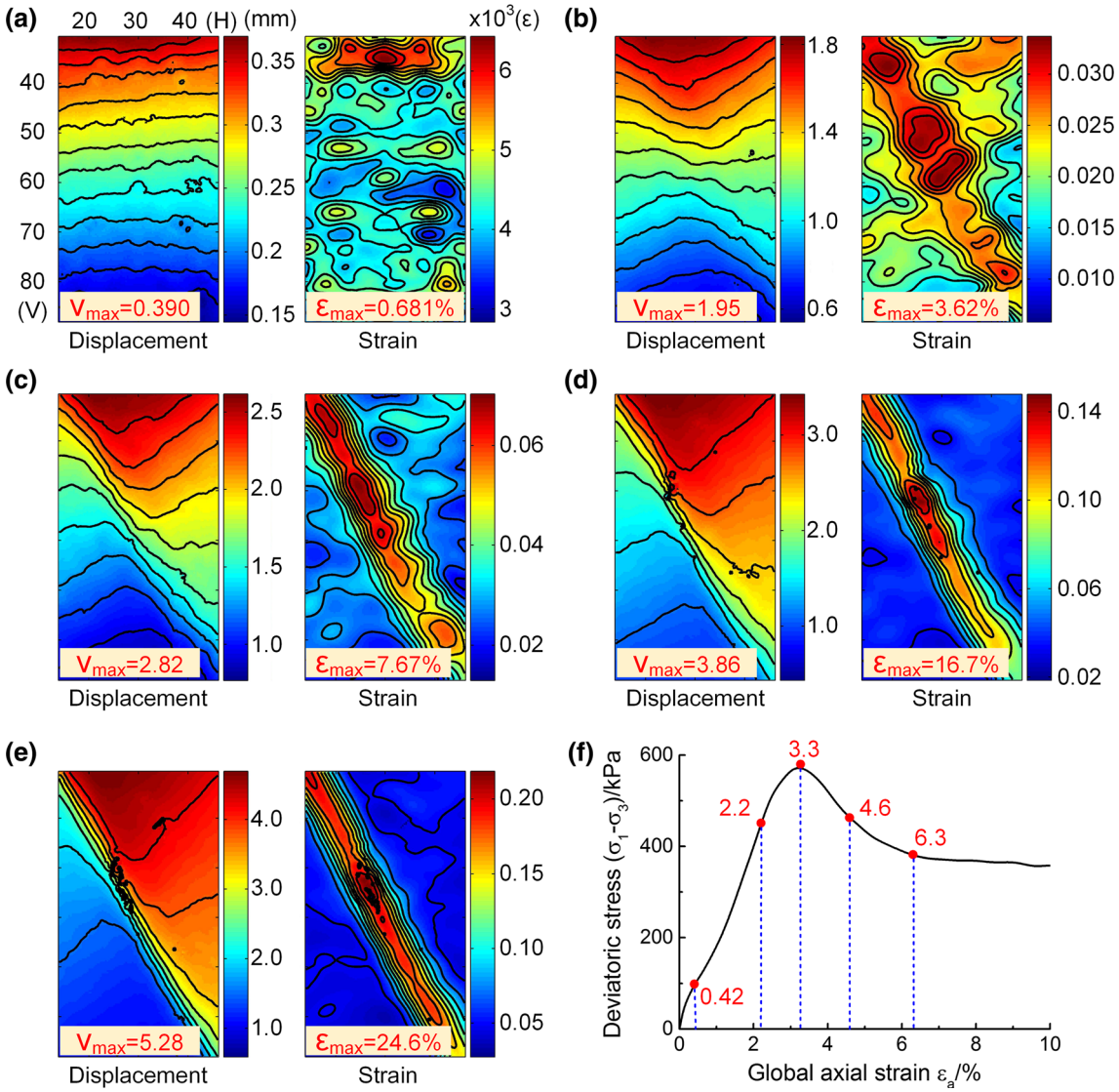

Fig. 7 **a–e** Incremental subset vertical displacement (unit: mm) contours and strain (unit: %) distribution diagrams through the course of test T2 which correspond to five moments in **f**. **f** The global stress–strain curve of T-2

calculation of displacement and strain. Approximately 70% of the specimen area in the camera view is covered by these points.

According to the experimental phenomenon, the entire loading procedure of the test can be divided into three states: pre-failure, in-failure and post-failure. In the pre-failure state, the specimen is fairly homogeneous, with no localized failure. The displacement contours are nearly flat. There are no larger deformed regions in the strain distribution diagram, as shown in Fig. 7a, and the value of vertical (axial) strain is from 3.5×10^{-3} to 6.8×10^{-3}. The deformation is relatively uniform. The process from onset to penetration of the shear band occurs in the in-failure state. As the loading increases, heterogeneity on the displacement contour in Fig. 7b is present. In the strain contour, the larger gradients, which correspond to local dense areas, appear. As shown in the strain distribution in Fig. 7b, there are multiple strain concentration regions. During test T-2, the peak stress occurred at approximately 3.26% global axial strain, as shown in Fig. 7f. Localized deformation was focused along conjugate planes at peak stress. However, a distinct behavioural trend is evidenced in Fig. 7c. The upper portion of the specimen was moving to the right and down in displacement contours. One obvious shear band is developing in the strain distribution diagram in Fig. 7d. The features of displacement and strain outside the shear band can be considered homogeneous. Figure 7b–d presents the development of shear band. This process is the in-failure stage. Finally, a narrow shear block (shear band) was formed between the upper and lower

portions. In this area, the maximum value of localized axial strain reached 24.6% at 6.3% global axial strain. The specimen was divided into two blocks. The displacement of the upper portion is much greater than that of the lower portion which is essentially motionless. However, their axial strain values are nearly equal. The average values outside the shear band are approximately 3%, which is much lower than the global axial strain, as shown in Fig. 7e. Thus, when an entire shear band has been formed, the specimen enters the post-failure state. As shown in Fig. 7a–f, the specimen can be considered a continuum element in the pre-failure state. Once a shear band is fully formed, local heterogeneous deformation reflects the constitutive response of the material. The displacement contours and strain distribution diagrams clearly reveal the evolution of the shear band during the test. The results show that the strain concentration region first appears in the middle of specimen. Gradually, it develops many concentration regions. Finally, a main shear band is formed.

4.2 Localized stress–strain behaviour and localized volumetric change

Shear damage can be originated from any point in the specimen. The point may be inside the specimen or on the surface of the specimen. Because the camera cannot view the internal points of the specimen, only the deformation of surface points can be obtained. In this paper, the evolution of the shear band is analysed through the deformation on the surface of specimens. Using the DIC algorithm, localized analyses can be achieved to determine the constitutive property of the sand. Figure 8a–f contrasts the globally measured response of test T-2 and test T-4 with the resulting localized stress–strain behaviour and localized volume strain. Four representative small regions are chosen: two regions are inside the shear band (No. 1 and No. 3); one region is in the upper portion (No. 2), and one region is in the lower portion (No. 4), as shown in Fig. 8a, d. Figure 8a–c corresponds to test T-2, and Fig. 8d–f corresponds to test T-4. To make the results more representative, the mean deformation of all points in one region is considered the localized deformation. The strain values are obtained from RG-DIC measurement results; the stress values are the average of the layer in which the region is located. The global and four regions' stress–strain curves in T-2 and T-4 are shown in Fig. 8b, e, respectively. The softening response of the regions inside the shear band is much more gradual than the corresponding global measurements. Every region is almost the same in pre-failure state. For the regions (No. 1 and No. 3) inside the shear band during the test process, the axial strain values have increased to approximately 20%, while the global axial strain reaches approximately 10%. For the regions (No. 2 and No. 4) outside the shear band, the axial strain values only reach approximately 3% at the end of the test. The global and four regions' volume strain curves in T-2 and T-4 are shown in Fig. 8c, f, respectively. The positive volume strain means contraction of the specimen, and the negative means extension. In test T-2, the global volumetric strain changes very little. The results are consistent with the hypothesis that the volume does not change in the saturation undrained test. Figure 8f shows that the volume of the specimen would increase in dry condition. The local volumetric strain of the region inside the shear band almost did not change in the pre-failure state and began to expand in the in-failure state. Finally, its localized volumetric strain reached 7%. However, the region outside the shear band was compressed by only approximately 1%. In test T-4 (Fig. 7f), the result is similar to that of test T-2, but the global volumetric strain in the dry condition is greater than that in the saturation condition.

4.3 The deformation of the shear band based on bifurcation theory

According to bifurcation phenomenon, the moments when the shear band begins and penetrates and the corresponding global axial strain can be obtained. Because the DIC can provide a large number of measurement points, it is very convenient to apply bifurcation theory. As shown in Figs. 7 and 8, the strain distribution and strain concentration zone can be obtained through the DIC algorithm. Taking T-2 as an example, the average axial strain outside the shear band and inside the shear band can be computed through the strain of all points. As shown in Fig. 9a, there is an obvious bifurcation point. In the initial stage, the two strain curves are almost the same. With sustained loading, the two strain curves develop in different directions. The bifurcation point is considered the beginning time of the shear band. With the development of the shear band, the strain probability density distribution of every histogram image will have one acute step at 3.25% strain value. Figure 9b and c illustrates that the strain probability density distribution versus the localized strain value of all measurement points at the global axial strain of 3.26% and 4.3%, respectively. The shapes of the two images in the range of the localized strain lower than 3.25% are very similar. This phenomenon arises because the main deformation of the specimen results from the shear band and the strain outside of the shear band does not increase considerably. According to the experimental results, a simple method for determining the penetrating time of the shear band is proposed. When the proportion of localized strain values that are less than 3.25% does not change, the specimen is considered to have reached its critical state. As shown in Fig. 9d, the specimen reaches its critical state at 4.4% global strain (curve turning

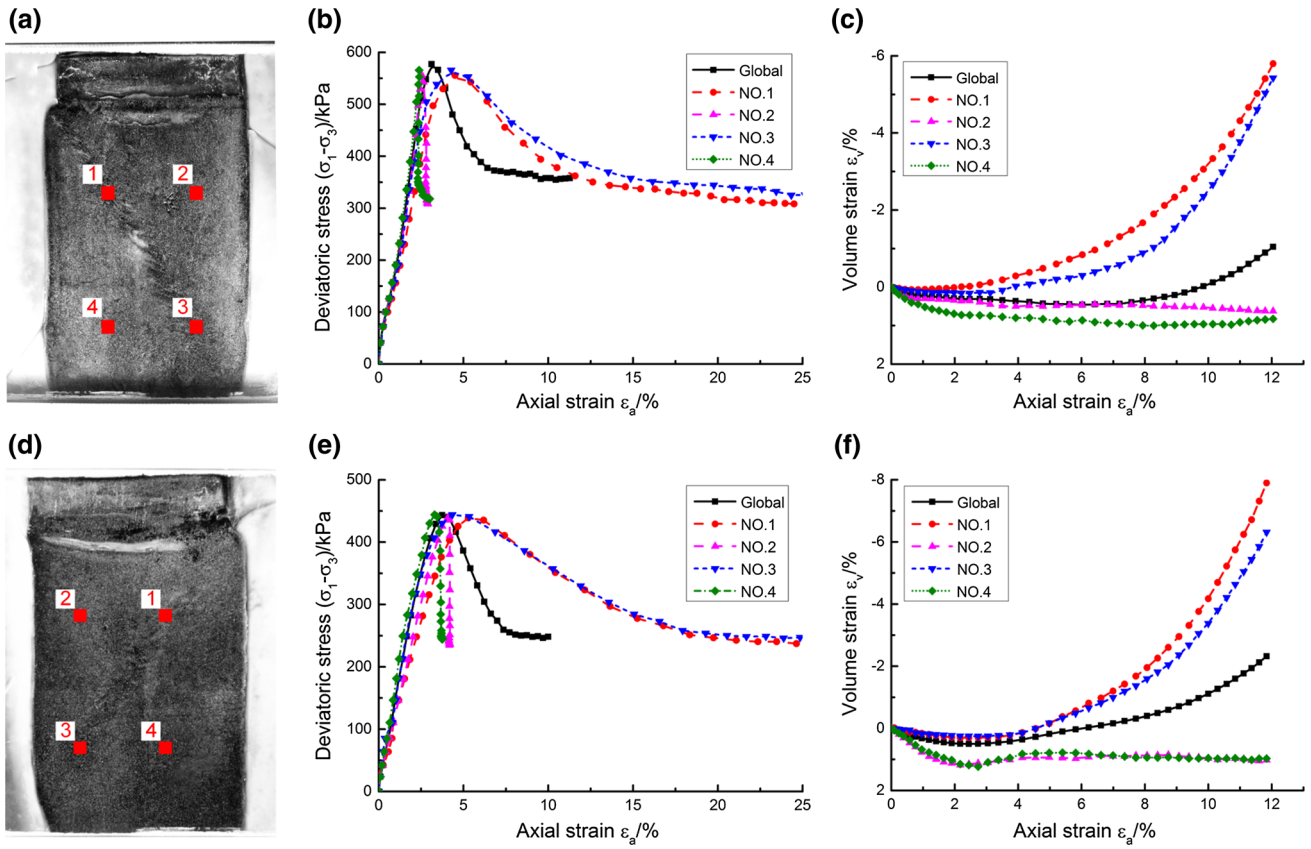

Fig. 8 **a**, **d**. Chosen four representative regions in the T-2 and the T-4 testing photograph, respectively. **b**, **e** Global and four regions' local stress–strain behaviour (T-2 and T-4). **c**, **f** Global and four regions' local volume strain (T-2 and T-4)

point). According to the above method, Fig. 10a–b shows the shear band beginning moment and penetrating moment in the global stress–strain curves regarding tests T1–T6.

In accordance with the observations of previous works, the start point of the shear band in sands is between 2.3 and 4.2% global strain and the formed point of the shear band is between 2.4 and 5.0% global strain [5]. From the above experimental data, the results using the DIC technique are more explicit than the previous results. With a conventional plane strain apparatus, the characterization of shear bands can be computed through two pairs of displacement transducers (LVDTs) [5]. Because of the limitation of the number of LVDTs, the conventional method cannot directly obtain the deformation distribution of specimens. The DIC measurement technique provides an easy and intuitive methodology to describe the characteristics of soils.

4.4 Shear band inclination and thickness

Table 2 lists measurements taken at the critical state of shear band inclination, β and theoretical solutions for shear band angle at critical state from Mohr–Coulomb theory, β_C; from Roscoe, β_R; and from Arthur, β_A:

$$\beta_C = 45^\circ + \frac{\phi'}{2} \tag{1}$$

$$\beta_R = 45^\circ + \frac{\psi}{2} \tag{2}$$

$$\beta_A = 45^\circ + \frac{\psi + \phi'}{4} \tag{3}$$

ϕ' is the inner friction angle which was obtained from Mohr strength criterion. Obviously, for all tests, shear band orientations are close to Arthur solution. According to geotechnical mechanics theory, the inner friction is the same between the saturated sand and dry sand. The measurement results support this resolution.

Single shear band is the most common style for shear band as shown in Fig. 7. Figure 11 presents its hypothesis model. The shear band inclination (β) and local deformation can be obtained by DIC. So, the dilatancy angle (ψ) also can be evaluated (Eq. 4). In Eq. 4 Δu_v is the incremental quantity in the vertical direction. Δu_h is the incremental quantity in the horizontal direction outside the shear

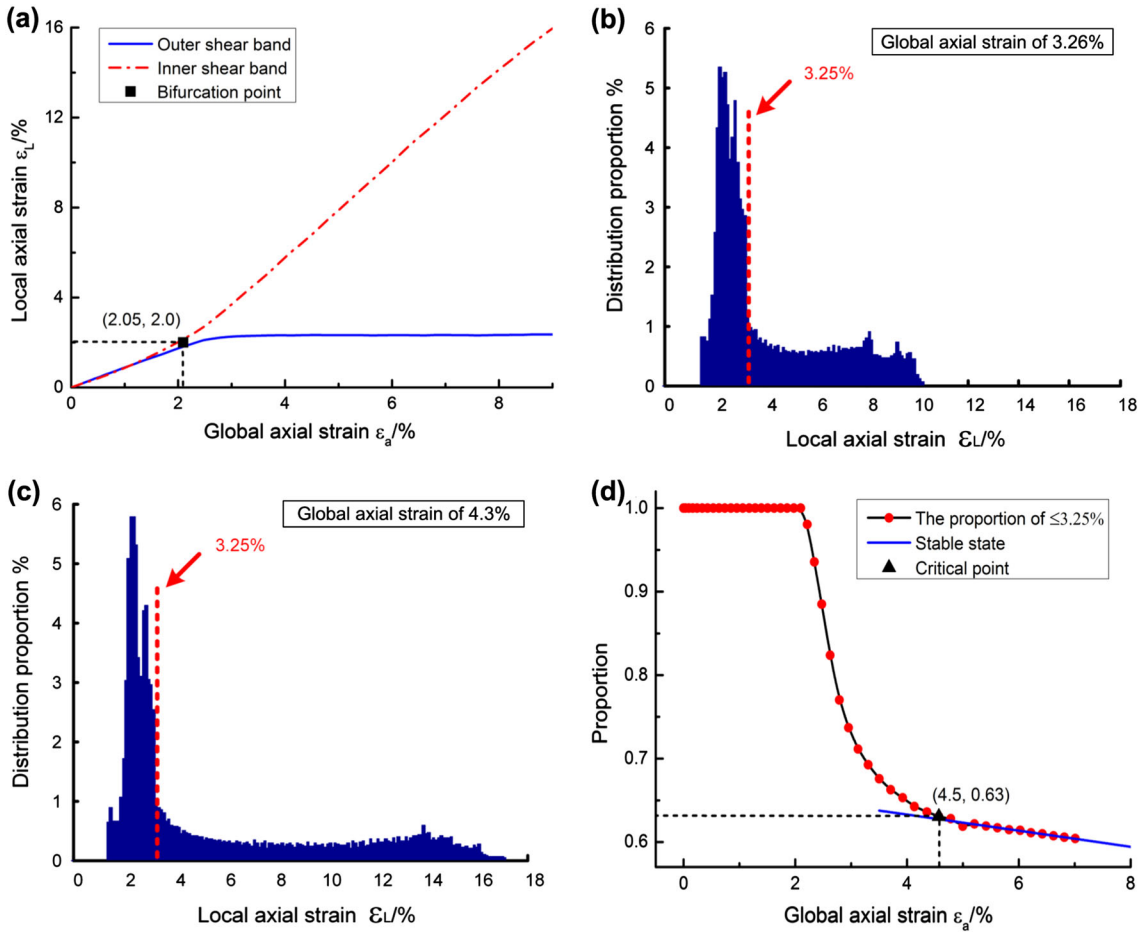

Fig. 9 **a** Average axial strain curve of outside shear band and inside shear band (T-2). **b**, **c** The strain probability density distribution at global axial strain of peak moment 3.26% and 4.3%, respectively. **d** The strain proportion which is less than 3.26% at every moment versus the global axial strain

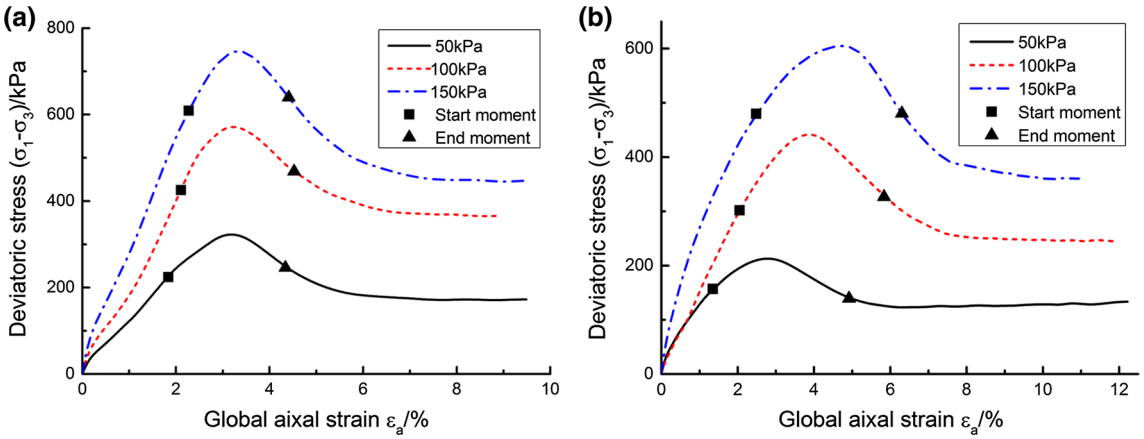

Fig. 10 **a**–**b** Moments when the shear band begins and penetrates of all tests in global stress–strain curves. **a** The results about T-1–T-3. **b** The results about T-4–T-6

band. ψ at the moment of shear band fully formed in every experiment is listed in Table 2.

$$\psi = \beta - \arctan\frac{\Delta u_v}{\Delta u_h} \tag{4}$$

The shear band thickness (T) is also summarized in the table and is normalized by the mean sand diameter, D_{50}. For the undrained test, the average shear band thickness is approximately $12D_{50}$ at the critical state. For the dry sand

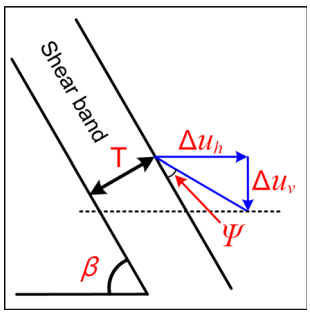

Fig. 11 Hypothesis model of single shear band

test, the value is approximately $17D_{50}$ (D_{50}= 0.37 mm). Figure 12 presents the methodology for evaluating the shear band thickness. The shear band inclination (β) can be obtained by DIC. Five lines are drawn in the vertical direction of the shear band (Fig. 12a). The strain values can be obtained in these five lines. The mean strain value of five lines is presented in Fig. 12b, and the distance between the points of maximum gradient in curve is treated as the shear band thickness (T).

5 Conclusions

In this paper, a new type of apparatus is used in plane strain testing. The flexible pressure vessels and hydraulic pressure control apparatus are adopted in the apparatus. These improvements can provide a more realistic simulation and more stable pressure compared to the conventional apparatus. An incremental reliability-guided digital image correlation (RG-DIC) is developed and used to evaluate the localized distribution of displacements and strains in sands. This technology is able to quantify shear band physical characteristics such as inclination, thickness and volumetric strains.

Based on the results of these tests, the following conclusions can be drawn:

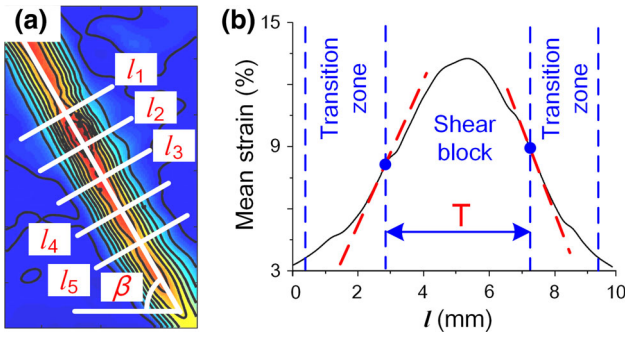

Fig. 12 **a**–**b** Principle for evaluating the shear band thickness. **a** The vertical strain distribution diagrams. **b** The mean strain value curve of five lines

1. RG-DIC is suitable to measure the large deformation in soils. The entire evolution of the shear band and the full-field data in the camera view can be obtained. Additionally, the measurement data regarding displacement and strain in the test can be used to create a video to reconstruct the deformation process, and the full-field measurement displacement data and strain data can provide more data for the simulation and theory of shear bands.
2. In pre-failure state, the specimen is fairly homogeneous. When localized failure appears, the specimen behaves as a structure. So, the global strain cannot quantify accurately the shear band behaviour of the soil; it just shows the combination of the characteristics of the soil in the failure zones and in the non-failure zones, especially in the in-failure and post-failure.
3. In both saturated sand and dry sand, the moments when the shear band begins and penetrates almost are the same. The moment when the shear band begins appears at the hardening stage, and the moment when the shear band penetrates appears at the softening stage. Under saturated and undrained conditions, the global volume changes little. However, the volume in the shear band does expand. This finding illustrates that there is volume exchange in the shear band in saturated sand. Regardless of whether the global volume changes, the results reveal that the volume inside the shear band expands during the compression.
4. The results illustrate that shear band inclination in medium-density sand is predicted by the Arthur solution. The local failure begins in the middle specimen. Gradually, the failure zone develops the shear band, which penetrates the specimen. According to the different deformation mechanisms, the failure process can be divided into three states: pre-failure, in-failure and post-failure.

Acknowledgments The work was supported the National Natural Science Foundation of China (No. 51309047).

References

1. Alikarami R, Andò E, Gkiousas-Kapnisis M, Torabi A, Viggiani G (2014) Strain localisation and grain breakage in sand under shearing at high mean stress: insights from in situ X-ray tomography. Acta Geotech 10(1):15–30. https://doi.org/10.1007/s11440-014-0364-6
2. Blaysat B, Grédiac M, Sur F (2016) Effect of interpolation in noise propagation from images to DIC displacement maps. Int J Numer Methods Eng. https://doi.org/10.1002/nme.5212
3. Desrues J, Chambon R, Mokni M, Mazerolle F (1996) Void ratio evolution inside shear bands in triaxial sand specimens studied by computed tomography. Géotechnique 46(3):529–546

4. Desrues J, Viggiani G (2004) Strain localization in sand: an overview of the experimental results obtained in Grenoble using stereophotogrammetry. Int J Numer Anal Methods Geomech 28(4):279–321. https://doi.org/10.1002/nag.338
5. Finno R, Harris W, Mooney MA, Viggiani G (1997) Shear bands in plane strain compression of loose sand. Geotechnique 47(1):149–165. https://doi.org/10.1680/geot.1997.47.1.149
6. Gao Y, Cheng T, Su Y, Xu X, Zhang Y, Zhang Q (2015) High-efficiency and high-accuracy digital image correlation for three-dimensional measurement. Opt Lasers Eng 65:73–80. https://doi.org/10.1016/j.optlaseng.2014.05.013
7. Grant BMB, Stone HJ, Withers PJ, Preuss M (2009) High-temperature strain field measurement using digital image correlation. J Strain Anal Eng Des 44(4):263–271. https://doi.org/10.1243/03093247jsa478
8. Hall SA, Bornert M, Desrues J, Pannier Y, Lenoir N, Viggiani G, BéSuelle P (2010) Discrete and continuum analysis of localised deformation in sand using X-ray μCT and volumetric digital image correlation. Géotechnique 60(5):315–322. https://doi.org/10.1680/geot.2010.60.5.315
9. Jang D-J, Frost JD (2000) Use of image analysis to study the microstructure of a failed sand specimen. Can Geotech J 37(5):1141–1149. https://doi.org/10.1139/t00-031
10. Kido R, Higo Y (2017) Evaluation of distribution of void ratio and degree of saturation in partially saturated triaxial sand specimen using micro x-ray tomography. Jpn Geotech Soc Spec Publ 5(2):22–27. https://doi.org/10.3208/jgssp.v05.006
11. Lewis JP (1995) Fast normalized cross-correlation. In: Paper presented at the vision interface
12. Lowe DG (2004) Distinctive image features from scale-invariant keypoints. Int J Comput Vis 60(2):91–110. https://doi.org/10.1023/B:VISI.0000029664.99615.94
13. Pan B, Dafang W, Yong X (2012) Incremental calculation for large deformation measurement using reliability-guided digital image correlation. Opt Lasers Eng 50(4):586–592. https://doi.org/10.1016/j.optlaseng.2011.05.005
14. Pan B, Xie H, Wang Z (2010) Equivalence of digital image correlation criteria for pattern matching. Appl Opt 49(28):5501–5509. https://doi.org/10.1364/AO.49.005501
15. Peters W, Ranson W, Sutton M, Chu T, Anderson J (1983) Application of digital correlation methods to rigid body mechanics. Opt Eng 22(6):738–742. https://doi.org/10.1117/12.7973231
16. Ra L, Fr J (2003) Digital image correlation to evaluate shear banding in dilative sands. Geotech Test J. https://doi.org/10.1520/GTJ11263J
17. Rechenmacher AL (2006) Grain-scale processes governing shear band initiation and evolution in sands. J Mech Phys Solids 54(1):22–45. https://doi.org/10.1016/j.jmps.2005.08.009
18. Rechenmacher AL, Abedi S, Chupin O, Orlando AD (2011) Characterization of mesoscale instabilities in localized granular shear using digital image correlation. Acta Geotech 6(4):205–217. https://doi.org/10.1007/s11440-011-0147-2
19. Shao LT, Liu G, Zeng FT, Guo XX (2016) Recognition of the stress–strain curve based on the local deformation measurement of soil specimens in the triaxial test. Geotech Test J 39(4):20140273. https://doi.org/10.1520/gtj20140273
20. Skarżyński Ł, Kozicki J, Tejchman J (2013) Application of DIC technique to concrete—study on objectivity of measured surface displacements. Exp Mech 53(9):1545–1559. https://doi.org/10.1007/s11340-013-9781-y
21. Stanier SA, Blaber J, Take WA, White DJ (2015) Improved image-based deformation measurement for geotechnical applications. Can Geotech J. https://doi.org/10.1139/cgj-2015-0253
22. Sutton M, Wolters W, Peters W, Ranson W, McNeill S (1983) Determination of displacements using an improved digital correlation method. Image Vis Comput 1(3):133–139
23. Thomas T (1958) Plastic flow and fracture in solids. J Math Mech 7:291–322
24. Vanne J, Aho E, Hamalainen TD, Kuusilinna K (2006) A high-performance sum of absolute difference implementation for motion estimation. IEEE Trans Circuits Syst Video Technol 16(7):876–883. https://doi.org/10.1109/TCSVT.2006.877150
25. Xu J, Moussawi A, Gras R, Lubineau G (2015) Using image gradients to improve robustness of digital image correlation to non-uniform illumination: effects of weighting and normalization choices. Exp Mech 55(5):963–979. https://doi.org/10.1007/s11340-015-9996-1
26. Yuan Y, Huang J, Peng X, Xiong C, Fang J, Yuan F (2014) Accurate displacement measurement via a self-adaptive digital image correlation method based on a weighted ZNSSD criterion. Opt Lasers Eng 52:75–85. https://doi.org/10.1016/j.optlaseng.2013.07.016
27. Zeng F, Shao L (2016) Unloading elastic behavior of sand in cyclic triaxial tests. Geotech Test J 39(3):20150171. https://doi.org/10.1520/gtj20150171
28. Zhang X, Li L, Chen G, Lytton R (2014) A photogrammetry-based method to measure total and local volume changes of unsaturated soils during triaxial testing. Acta Geotech 10(1):55–82. https://doi.org/10.1007/s11440-014-0346-8